CHEMISTRY OF MATERIALS

pubs.acs.org/cm

Article

Self-Assembled Bilayer Microstructure Improves Quasi-2D Perovskite Light-Emitting Diodes

Tanghao Liu,[#] Qi Wei,[#] Songhua Cai,[#] Bingchen He, Zhenhuang Su, Zhipeng Zhang, Yalan Zhang, Hua Zhou, Gang Wang, Yulan Huang, Jiahao Ren, Yuanyuan Zhou,[*] and Guichuan Xing[*]

Cite This: *Chem. Mater.* 2022, 34, 10435−10442

Read Online

ACCESS | Metrics & More | Article Recommendations | Supporting Information

ABSTRACT: Metal halide perovskites with quasi-2D crystal structures have shown excellent electroluminescent properties due to the inherently confined charge diffusion and efficient radiative recombination. But quasi-2D perovskite films can exhibit complex phase characteristics that need to be tailored for achieving high-performance light-emitting diodes (LEDs). Here, we report a unique quasi-2D perovskite thin film structure featuring a 3D perovskite bottom sublayer underneath a mixed 2D−3D perovskite composite upper sublayer, as imaged by low-dose scanning transmission electron microscopy. We demonstrate that the incorporation of a potassium bromide additive can trigger the self-assembly of multiphase perovskite grains toward this bilayer microstructure, probably due to its ability to create heterogeneous nucleation templates for the crystallization of 3D perovskite grains on the precursor−substrate bottom interface. The external quantum efficiency of quasi-2D perovskite LEDs is significantly improved by this bilayer film microstructure. By probing the carrier dynamics using transient absorption spectroscopy, we attribute the LED performance enhancement to the accelerated carrier transfer and recombination across the bilayer film microstructure.

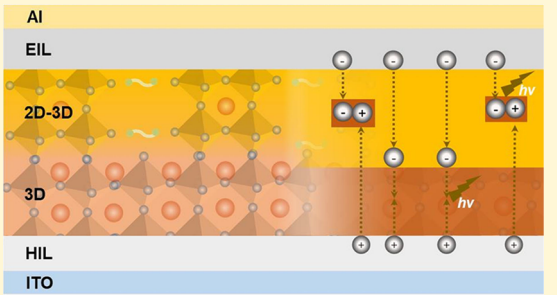

In the recent years, perovskite-based LEDs (PeLEDs) have attracted enormous research interest and the field has witnessed their rapid development along with the progress in understanding their composition and microstructures.[1−8] The highest external quantum efficiency (EQE) of PeLEDs has now reached 28%.[9] Conventional 3D perovskites have been used in the early stage of PeLEDs, but the performance has been relatively limited. In this regard, quasi-2D perovskites have attracted more attention and possess the advantages of shortened charge diffusion lengths and higher exciton binding energies.[6,10] In particular, quasi-2D perovskites are inherently formed with mixed 2D and 3D (perovskite layer number $n = \infty$) phases of various layer numbers (n) when processed into thin films. The charge funneling from 2D phases to the 3D phase can compete with the trap filling, which is of vital importance for suppressing nonradiative recombination and improving electroluminescence (EL) efficiencies.[11,12] Nevertheless, the solution growth of different quasi-2D perovskite phases is relatively complex, frequently leading to unfavored microstructures that strongly influence the charge-carrier dynamics.[13−18] Therefore, there is a need for the rational design of quasi-2D perovskite film microstructures via tailored synthesis.

In general, the following principles may be followed for designing high-performance quasi-2D PeLEDs: (i) lower-n 2D phases should be suppressed because their low conductivities hinder the charge injection and charge funneling to the 3D phase; (ii) lower-n 2D phases should form intimate contact interfaces with 3D or higher-n 2D phases to favor the charge transfer. (iii) The emission centers, which are primarily based on 3D phases,[4,12] should locate closer to the hole injection layer (HIL) in a p-i-n PeLED device, as the potential barrier of hole injection is usually larger than that of the electron injection.[19] While there are some studies addressing the first two,[13,20] the third design principle has been rarely considered. In this work, we introduce potassium bromide (KBr) as a solution-processing additive for the attainment of our quasi-2D perovskite film goal. Note that we have chosen a typical quasi-2D perovskite precursor composition of $PEA_2(FA_{0.9}Cs_{0.1})_2Pb_3Br_{10}$ for the proof-of-concept demonstration. We consider two possible beneficial factors related to KBr additive for the film synthesis. First, KBr exhibits a 3D cubic crystal symmetry with a lattice parameter of around 0.6 nm, which is close to that of the 3D cubic FA-Cs tribromide perovskite phase ($FA_{0.9}Cs_{0.1}PbBr_3$). During the solution crystallization, some KBr phases possibly precipitate first at the precursor−substrate bottom interface. They serve as nucleation templates for the sequential growth of larger 3D

Received: July 31, 2022
Revised: November 2, 2022
Published: November 15, 2022

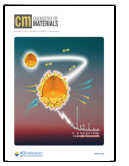

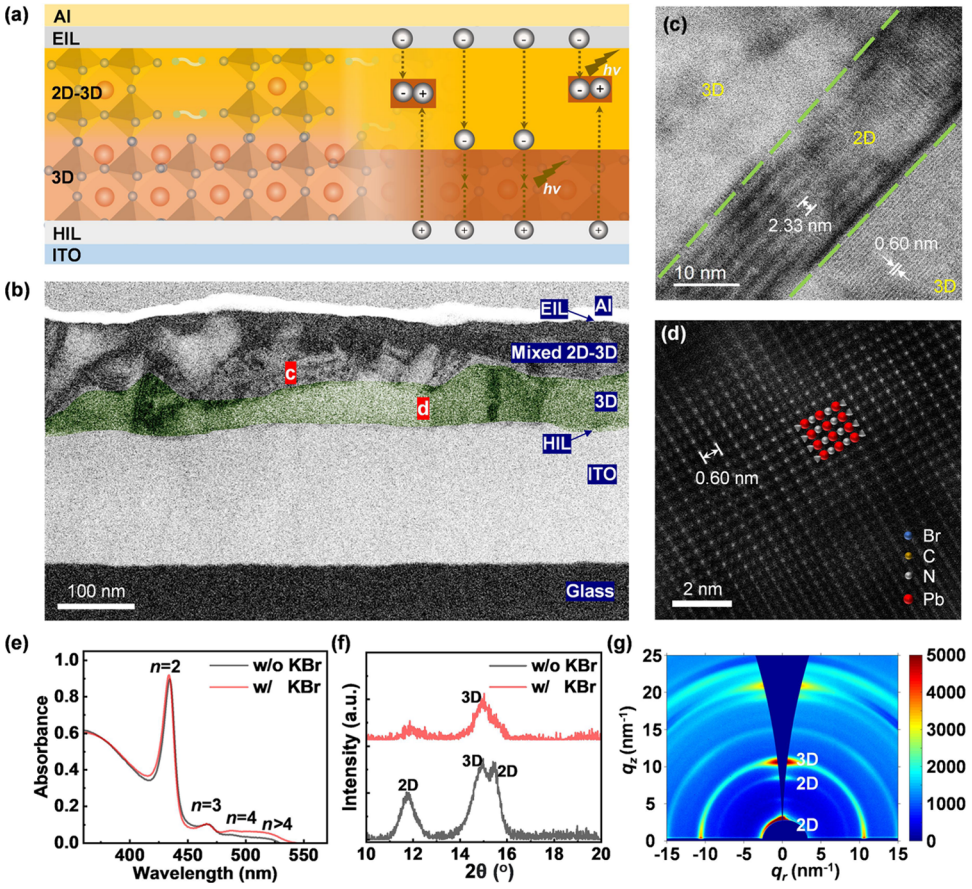

Figure 1. (a) Schematical structure of the KBr-incorporated quasi-2D perovskite film. (b) Low-magnification cross-sectional scanning transmission electron microscopy-high-angle annular dark field (STEM-HAADF) image of the KBr-incorporated quasi-2D perovskite film. (c−d) High-resolution STEM-HAADF image taken from (c) the 2D−3D mixed-phase region in the upper sublayer and (d) the 3D perovskite grain in the bottom sublayer as labeled in (b). (e) UV−vis absorption spectra and (f) X-ray diffraction (XRD) patterns of KBr-free and KBr-incorporated quasi-2D perovskite films. (g) Grazing-incidence wide-angle X-ray scattering (GIWAXS) pattern of the KBr-incorporated quasi-2D perovskite film.

perovskite grains on the HIL that will then become near-HIL emission centers. KBr may be also dispersed in the precursor solution, initializing the heterogeneous nucleation of finer 3D perovskite within the film bulk.[21] Second, K^+ ions can passivate ionic defects in perovskites through strong interactions with halide anions, which can not only mitigate nonradiative recombination in 3D perovskites but also increase the film conductivity to facilitate carrier injection.[21−25] Based on these two factors, we observe that the KBr incorporation in the precursor solution leads to the evolution of a quasi-2D perovskite film structure with a bottom sublayer of aggregated 3D perovskite grains and an upper sublayer of a 2D−3D phase mixture. PeLEDs adopting this interesting film structure show significant enhancement in EQE compared to the regular quasi-2D perovskite film structure, which is attributed to accelerated carrier transfer as reflected from comprehensive transient absorption (TA) spectroscopic studies. This work presents an opportunity leveraging the versatile film microstructures of quasi-2D perovskites for innovations toward optoelectronic device advances.

■ MICROSTRUCTURAL CHARACTERIZATION

Figure 1a schematically illustrates the unique device structure of KBr-incorporated PeLED, where the perovskite film with a bilayer microstructure is sandwiched between the poly(3,4-ethylenedioxythiophene)-poly(styrenesulfonate) (PEDOT:PSS) HIL and 2,2′,2″-(1,3,5-Benzinetriyl)-tris(1-phenyl-1-*H*-benzimidazole) (TPBi) electron injection layer. In the perovskite layer, the 2D−3D mixed perovskite upper sublayer stacks on the 3D perovskite bottom sublayer. The energy level diagram for this device structure is schematically shown in Figure S1. The conduction band minimum of TPBi is higher than that of perovskite. Thus, the electron injection from TPBi to perovskite is energetically facile. However, the valence band maximum of PEDOT:PSS is higher than that of perovskite, creating a potential barrier that hinders the hole injection. Such a potential barrier can be reduced when a 3D perovskite layer is inserted between PEDOT:PSS and 2D perovskite phases. Also, 3D perovskite is known to exhibit a relatively higher conductivity,[20] which can further facilitate the hole injection. Based on these considerations, we expect the radiative recombination can be boosted in both the 3D perovskite bottom sublayer and mixed 3D−2D perovskite top sublayer, as schematically illustrated in Figure 1a.

Scanning transmission electron microscopy (STEM) characterization is used to confirm the cross-sectional microstructure of perovskite films. We used focused ion beam (FIB) to prepare the PeLED device cross-section specimen followed by the deposition of a 10 nm thick amorphous carbon layer to improve the sample stability under an electron probe. This method has been previously demonstrated for reliable atomic-scale characterization of perovskites.[26] Figure 1b is a typical

https://doi.org/10.1021/acs.chemmater.2c02340
Chem. Mater. 2022, 34, 10435−10442

low-magnification STEM image showing the cross-section of a KBr-incorporated PeLED device with each layer delineated. Based on the image contrast, we observed the mixture of thin lamella (in lower contrast) and relatively smaller grains (in higher contrast) distributes at the upper part of the film, while large grains (in higher contrast) mainly locate at the film bottom. To determine the phases of these lamella and grains, we acquired low-dose high-resolution STEM images (Figure 1c,d) at two typical locations in the top and bottom sublayers of perovskite (labeled in Figure 1b). The electron beam current for the imaging is as low as less than 5 pA. For the top sublayer (Figure 1c), the lattice fringes of the observed thin lamella show an interlayer distance of 2.33 nm, corresponding to that of the $n = 3$ phase. Beside the 2D perovskite lamella, 3D perovskite grains with a measured interplane distance of 0.60 nm is shown. For the bottom sublayer (Figure 1d), owing to the enhanced crystallinity and sample integrity, the atomic-scale crystal structure of the grain is even visualized, unambiguously demonstrating the 3D perovskite phase (Figure 1d). These 3D perovskite grains are closely packed in the bottom sublayer, showing a quasi-polycrystalline morphology (Figure S2). These results confirmed the consistence between the real and schematic microstructures of the KBr-incorporated perovskite film. For comparison, a control quasi-2D perovskite film (in the device setting) is also prepared without KBr incorporation. The thicknesses of both perovskite films are similar (~170 nm) as measured by a step profiler (Figure S3). The microstructure of the KBr-free perovskite film is also imaged using STEM (Figure S4). As expected, it exhibits a uniform mixture of low-contrast 2D and high-contrast 3D phases within the entire film. No distinguishable 3D perovskite bottom sublayer is observed. The bilayer microstructure can be also reflected from the significant differences between the photoluminescence (PL) characteristics of KBr-incorporated films measured from bottom and top sides (Figure S5).

The phase distributions in the perovskite films with and without KBr incorporation were also revealed using UV−vis absorption spectroscopy. As shown in Figure 1e, the absorbances of the two films are similar in the sub-470 nm wavelength range, but in the wavelength range of 470−530 nm, the absorbance of the KBr-incorporated perovskite film is obviously higher, which can be attributed to more populated higher-n phases. Figure 1f compares the XRD patterns of the films with and without KBr incorporation. The diffraction peaks at around 11.2° to 15.1° are characteristic of 2D perovskites and the diffraction peak at 14.9° corresponds to (100) reflection of the 3D perovskite.[8,27] For the KBr-free film, the XRD peak intensities for 2D perovskites are close to those for 3D perovskites. Once KBr is incorporated, the relative intensities of XRD peaks for the low-n 2D perovskites become significantly weaker than those for 3D perovskites. This further confirms that KBr incorporation suppresses the formation of 2D perovskites in the film. This is consistent with the STEM observation showing 3D perovskite grains as the dominant "building block" for the KBr-incorporated perovskite film. The GIWAXS pattern of the KBr-incorporated perovskite film is shown in Figure 1g, revealing strong texture characteristics for both 3D perovskite grains and 2D perovskite lamellas, favoring carrier injection and transport.[15] In contrast, highly random lamella or grain orientations were observed for the KBr-free perovskite film (Figure S6). The thermal stability of the perovskite film is also improved with KBr incorporation, which attests to the 3D perovskite dominated film composition. It is known that the van der Waals bonding in 2D perovskites is weaker than the ionic bonding in 3D perovskites.[28] In-situ GIWAXS patterns were collected for both films being annealed in a nitrogen atmosphere at an elevated temperature of 100 °C. As shown in Figure S7, the (100) diffraction peak of the KBr-incorporated film can maintain 70% of its initial intensity for 1500 s as compared with only 300 s for the KBr-free case. The exact formation mechanism of the KBr-induced bilayer film microstructure is not clear at this time, since it can involve complex phase formation and transformation during the spin-coating and annealing steps. In the future, we hope to leverage in-situ, multimodal characterization to clarify the mechanism and tailor the bilayer film microstructure in a more precise manner, which is within the scope of frontier fundamental research on perovskites.[29]

Optical Properties. The PL spectra of KBr-free and KBr-incorporated perovskite films are shown in Figure S8a. The PL intensity is increased after the KBr incorporation, which may can be attributed to increased emission centers and lower trap density. The PL quantum yields (PLQYs) of both films are further compared. Figure S8b shows the PLQY statistics based on 10 measurements for each type of film samples. The KBr incorporation improves the average PLQY from 39 to 45%. TRPL spectra of both films were tested (Figure 2a), which can

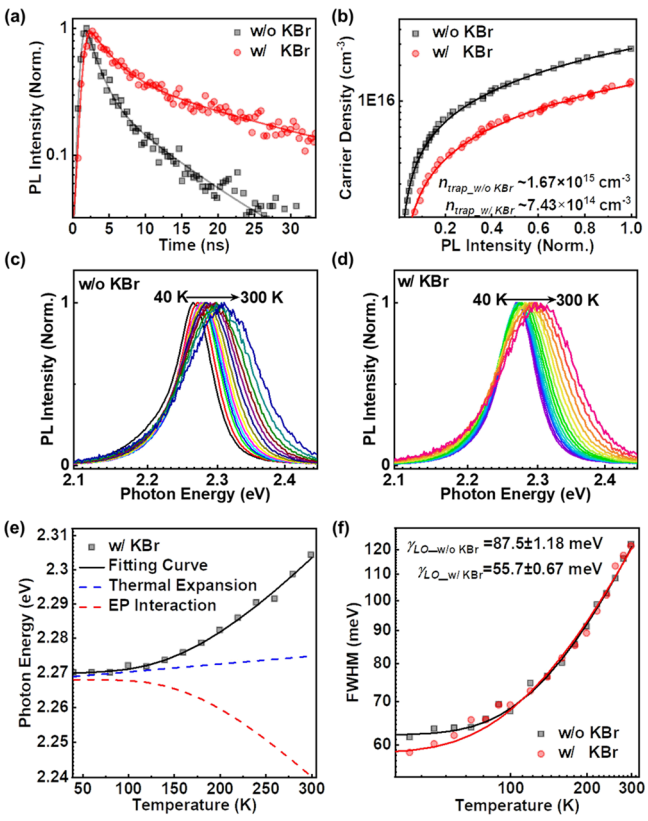

Figure 2. (a) Time-resolved PL (TRPL) spectra for KBr-free and KBr-incorporated perovskite films under low pump fluence excitation. (b) Pump fluence-dependent PL intensity, the fitted trap-state density for KBr-free and KBr-incorporated is 1.67×10^{15} cm^{-3} and 7.43×10^{14} cm^{-3}, respectively. (c,d) Temperature-dependent PL emission of KBr-incorporated perovskites from 40 to 300 K. (e) Evolutions of PL emission peak energy with temperature extracted out from (c,d). (f) Plots of PL emission peak full width at half maximum (FWHM) as a function of temperature for KBr-free and KBr-incorporated perovskite films.

https://doi.org/10.1021/acs.chemmater.2c02340
Chem. Mater. 2022, 34, 10435−10442

be described using biexponential functions (see fitting parameters in Table S1). The KBr-incorporated perovskite film shows a much longer average carrier lifetime (τ_{avg}: 7.8 ns; as compared to 2.8 ns for the KBr-free case), further confirming the reduced trap density and thus nonradiative recombination. Pump fluence-dependent PL spectra were acquired to quantify the trap densities of both films (Figure 2b). Under a low pump fluence, the relationship between the initial photogenerated carrier density (n_c) and PL intensity can be described using the equation,

$$n_c = n_{TP}(1 - e^{-I_{PL}/k}) + I_{PL}/k$$

where n_{TP} is the trap density, k is a constant that refers to the radiative recombination coefficient. The value of trap density (n_{TP}) can be obtained by fitting the experimental data with this equation.[7,13] Based on this, the trap densities of KBr-free and KBr-incorporated perovskite films are quantified as 4.5×10^{15} cm^{-3} and 2.2×10^{15} cm^{-3}, respectively.

To further understand the enhancement of PL properties by KBr incorporation, we carried out a low-temperature PL analysis. Figure 2c,d shows the normalized temperature-dependent PL spectra of KBr-free and KBr-incorporated perovskite films, respectively. For both films, with the increase of temperature from 40 to 300 K, the PL peaks gradually blue-shift and the FWHM increases. In general, the temperature dependence of the bandgap can be described by the following expression:

$$E_g(T) = E_0 + A_{TE}T - A_{EP}\left(\frac{2}{\exp\left(\frac{E_{avo}}{k_BT}\right) - 1} + 1\right) \quad (1)$$

Two factors contribute to the photon energy shift in perovskites. The first factor is the thermal expansion (TE) of the lattice (the first term in equation) with the increase of temperature. The interaction between the p orbit of Br and the s orbit of Pb will be reduced due to the thermal induced expansion, and thus resulting in a decrement of the valance bandwidth. The second factor is the exciton−phonon (EP) interaction. In eq 1, E_0 is the unrenormalized bandgap, A_{TE} is the weight of the TE, A_{EP} is the weight of electron−phonon interaction, and E_{avo} is the average optical phonon energy. The fitted A_{TE}, A_{EP}, and E_{avo} for both samples are listed in Table S2.

Figure 2e shows the temperature-dependent FWHM of the KBr-incorporated perovskite film. It clearly shows that the linear-increased PL peak can be derived from the domination of TE at low temperature, while EP interaction is negligible due to the insubstantially populated optical phonon modes. In a higher temperature region, the optical phonon modes are appreciably populated, leading to a severe negative influence. The A_{EP} is reduced from 251 to 153 meV by doping KBr in perovskites, which indicates that the TE of lattice plays a significant role in the photon energy shift in KBr-incorporated perovskite rather than the KBr-free perovskite. The reduced A_{EP} indicated that the EP coupling was weakened in the KBr-incorporated perovskite.

We then estimated the relative strength of the Fröhlich coupling in perovskite samples by using a simplified model to fit the experimental data:

$$\Gamma(T) = \Gamma_0 + \frac{\gamma_{LO}}{\exp^{(\hbar\omega_{LO}/k_BT)} + 1} \quad (2)$$

where, Γ_0 is a temperature invariant parameter as previous been used for quantum wells and γ_{LO} is the longitudinal optical (LO)-phonon coupling strength. We assumed $\hbar\omega_{LO}$ is the LO phonon energy. The broadening of perovskite emission above 100 K was fairly linear in both KBr-free and KBr-incorporated films. Through eq 2, we estimated the relative strength of the Fröhlich phonon coupling arising in two recombination pathways in perovskite films. γ_{LO} is revealed to be 87.5 ± 1.18 meV for the KBr-free perovskite and 55.7 ± 0.67 meV for the KBr-incorporated perovskite. Moreover, the comparison of temperature-dependent PL intensities from KBr-free and KBr-incorporated perovskites is shown in Figure S9. The thermal activated PL quenching is described by an Arrhenius expression: $I = I_0(1 + Ae^{-E_b/K_BT})$. The exciton binding energy (E_b) can be determined by fitting the temperature-dependent PL intensity. With the increase of temperature, heat induced exciton disassociation leads to the decrease of PL intensity. I_0 is the PL intensity at 0 K and K_B is the Boltzmann constant (1.38×10^{-23} J/K). The E_b of the KBr-incorporated perovskite film is 122 meV, slightly lower than that of the KBr-free perovskite film (142 meV). In the low-temperature region, the PL intensity of the KBr-incorporated perovskite is consistently higher than that of the KBr-free perovskite. Typically, electron−phonon coupling is thought to show an impact on the electronic transition rate. For instance, the stronger electron−phonon the coupling strength, the more pronounced the vibrational modes coupled with the electron excitations, corresponding to faster nonradiative recombination and poor light emission.[30] The modulation of EP interactions favors PL emission by converting excitons in EP interactions into radiative recombination. Through low-temperature PL analysis, the weaker electron−phonon interactions in the KBr-incorporated perovskite certainly contribute to the better light emission properties (which means less nonradiative recombination). Moreover, reduced electron−phonon coupling in perovskites could improve the mobility and their stability against electric fields in the corresponding crystals, which may be also beneficial to application in light emission devices.[31]

Charge-Carrier Dynamics. TA is then employed to investigate the phase distribution and charge-carrier dynamics in quasi-2D perovskite films (Figure S10). The PB peaks at 435, 467, 489, and ∼525 nm are corresponding to n = 2, n = 3, n = 4, and n = ∞ perovskite phases, respectively. For the KBr-free film, the n = 2 peak was much stronger than the n = ∞ peak. While for the KBr-incorporated perovskite film, the n = ∞ peak was relatively stronger, indicating the increased amount of 3D phase after the incorporation of KBr.

The detailed bleaching kinetics of n = 2, 3, and 4 and n = ∞ phases in two perovskite films were extracted and fitted with a multiexponential function (Figure 3). Fitted parameters of n = 3 and n = ∞ PB kinetics are shown in Tables S3 and S4. For all samples, PB peaks of all phases rose rapidly within 0.2 ps after pumped by the excitation laser. Then, n = 2, 3, 4 peaks decreased gradually and the 3D peak kept rising simultaneously till ∼70 ps. It indicates the charge funneling from 2D phases to the 3D phase, which can be divided clearly into a rapid step and a slow step. The EL property of the quasi-2D perovskite film is strongly dependent on the charge funneling process. Due to the limited conductivity of 2D perovskites, the charge transfer from the inert to the surface is slow. Therefore, the rapid step (0.2−0.5 ps) is dominated by the charge transfer at the 2D/3D interface, while the subsequent slow step (0.5−

https://doi.org/10.1021/acs.chemmater.2c02340
Chem. Mater. 2022, 34, 10435−10442

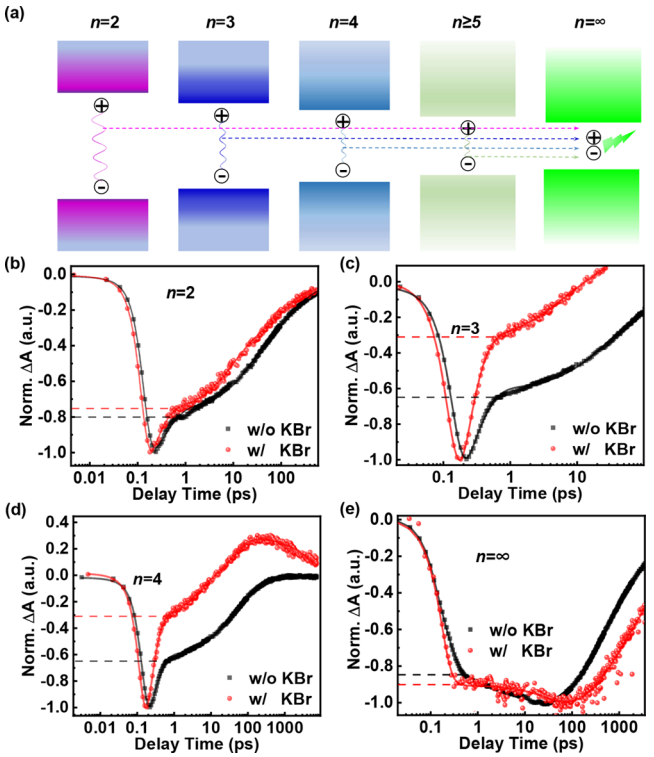

Figure 3. (a) Schematic illustration of the charge-carrier funneling behaviors in a quasi-2D perovskite film containing various 2D and 3D (i.e., $n = \infty$) phases. (b–e) Photobleaching (PB) kinetics of $n = 2$ (b), $n = 3$ (c), $n = 4$ (d), and $n = \infty$ (e) phases in KBr-free and KBr-incorporated perovskite films.

70 ps) is mainly ascribed to the charge transfer from the inert 2D phases to the 3D phase.

In the rapid funneling step, $n = 2$, 3, and 4 peaks of the KBr-incorporated film decreased to 76, 31, and 5% of their maximum values, respectively, while $n = 2$, 3, and 4 peaks of the KBr-free film decrease to 81, 65, and 29% of their maximum values, respectively. Meanwhile, $n = \infty$ peaks of KBr-incorporated and KBr-free films rose to 90 and 86% and the $n = \infty$ peak of the KBr-incorporated film rose relatively faster. Based on these comparisons, several conclusions can be drawn. First, the charge transfer from higher-n phases to 3D phase was much more efficient than lower-n phases to the 3D phase in this step. Second, the rapid charge funneling process in the KBr-incorporated film was more efficient than that in the KBr-free film, which was reasonably induced by the suppressed low-n phases in the KBr-incorporated perovskite film. In the subsequent slow funneling step, $n = 2$, 3, and 4 peaks of both films kept decreasing. In addition, $n = \infty$ peaks of KBr-incorporated and KBr-free films rose to their maximum at 70 and 25 ps, respectively. It means the charge funneling process lasted longer in the KBr-incorporated film. In this way, more charge carriers could be injected into 3D emission centers in the KBr-incorporated film. After the charge funneling process, charge carriers in $n = \infty$ phase recombined and produced green emission gradually. The radiative recombination lifetime of the KBr-incorporated perovskite film was longer than that of the KBr-free perovskite film, confirming the structural benefits from the bilayer film microstructure.

Device Performance. PeLEDs were fabricated with a device structure of indium tin oxide (ITO) /PEDOT:PSS/perovskite/TPBi/LiF/Al. Figure 4a,b compares the current density–voltage (J–V) and luminance–voltage (L–V) curves of KBr-free and KBr-incorporated PeLEDs, respectively. When the driving bias is lower than 4.5 V, the J and L of KBr-incorporated PeLED were higher than those of the KBr-free PeLED, indicating a lower charge injection barrier in the KBr-incorporated PeLED. When the driving bias is higher than 4.5 V, the current density of the KBr-free PeLED become comparable with that of KBr-incorporated PeLED. Nevertheless, the luminance of the KBr-free PeLED starts to be lower than that of KBr-incorporated PeLED, and the difference becomes even larger with an increase of V. This may indicate reduced Auger recombination in KBr-incorporated PeLED.[32] The CE and EQE of the best-performing KBr-free PeLED and KBr-incorporated PeLED are compared in Figure 4c,d. The highest CE and EQE of KBr-free PeLED were 27.9 cd/A and 8.2%, which are improved to 46.9 cd/A and 13.8% by KBr incorporation, respectively. The statistical distributions of PeLED performance are presented in Figure 4e based on the EQEs of 50 devices for each case, confirming the

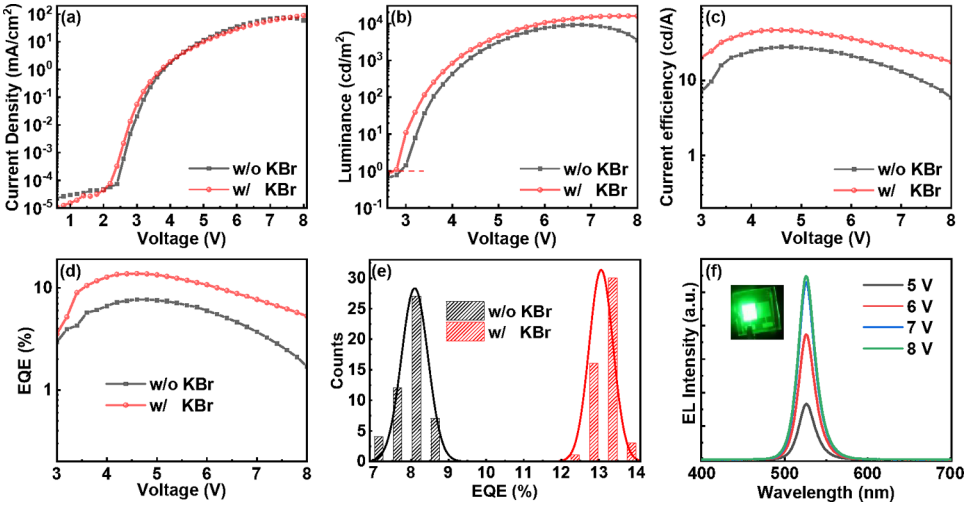

Figure 4. (a) J–V curves, (b) L–V curves, (c) current efficiency (CE)-V curves, (d) EQE-V curves, and (e) EQE statistics of KBr-free and KBr-incorporated PeLEDs. (f) EL spectra of the best-performing KBr-incorporated device under various bias.

https://doi.org/10.1021/acs.chemmater.2c02340
Chem. Mater. 2022, 34, 10435–10442

reproducibility of the KBr-induced improvement. Notably, KBr-incorporated PeLEDs exhibit a narrow EQE distribution with a small variation of only 0.5%. Figure 4f shows the EL spectra of the champion device under various driving biases. The emission peaks are centered at 528 nm, and the FWHMs are as low as around 22 nm, demonstrating high green color purity.

CONCLUSIONS

In closing, KBr incorporation in the solution processing of quasi-2D perovskite films significantly improves the performance of resultant PeLEDs. The beneficial modulation of the film microstructure and phase distribution underpins the device improvement. With KBr incorporation, a smaller content of 2D perovskite phases can be achieved in the film while the growth of 3D perovskite phases can be promoted at preferred film regions. This contributes to facilitating the charge injection, increasing emission centers, and reducing trap densities. In addition, the 3D perovskite layer at the film bottom region is favorable for hole injection. As a result, the KBr-incorporated PeLEDs can deliver a high quantum efficiency of 13.8% with excellent device reproducibility. This work points out to numerous research opportunities on microstructural innovations in quasi-2D perovskite films for more efficient light emission.

EXPERIMENTAL SECTION

Chemical and Materials. $PbBr_2$ (99.8%), formamidinium bromide (FABr, 99.8%), cesium bromide (CsBr, 99.8%) phenylethylamine bromide (PEABr), PEDOT:PSS 4083, and TPBi were purchased from the Xi'an Polymer Light Technology Corp., China. Lithium fluoride (LiF) and KBr (99.99%) were purchased from Sigma Aldrich, USA. Dimethylsulfoxide (DMSO, 99.8%) and chlorobenzene (CB, 99.8%) were purchased from Acros Organics, USA. All chemicals are used as received without further purification.

Preparation of Quasi-2D Perovskite Films. For preparing the control quasi-2D perovskite precursor solution with a Pb^{2+} concentration of 0.48 M, 64.6 mg PEABr, 6.8 mg CsBr, 36.0 mg FABr, and 176.2 mg $PbBr_2$ were dissolved in 1 mL DMSO solvent. For preparing the KBr-incorporated perovskite precursor solution, 5.8 mg KBr was added into the control precursor solution. The solutions were stirred for at least 60 min and filtered with 0.22 μm filters before use. Quasi-2D perovskite films were deposited by spin-coating the precursor solution at 3000 rpm for 120 s and during this step, and 100 μL CB was dropped at 30 s after the start of the spin-coating. The spun films were then transferred to a hot plate and annealed at 90 °C for 60 min.

Structural Characterization. For TEM characterization, the cross-section specimens of perovskite films were prepared using a dual-beam FIB nanofabrication platform (Helios 600i, Thermo Fisher). A Pt protection layer was first deposited on the top surface of the sample followed by etching the surrounding area to form the specimen lamella. The operation voltage of gallium ion beam is 30 kV, and the working current is 0.1 to 24 nA for lamella processing. The lamella was then lifted out from the substrate and in-situ transferred to a TEM half-ring lift-outgrid inside the FIB chamber. The observation area of the lamella was thinned to less than 100 nm with a 40 to 790 pA gallium ion beam. To minimize the damage induced by ion implantation to the sample lamella, a fine milling and polishing process was adopted by using a gallium ion beam with acceleration voltage down to 1 kV and 72 pA working current to remove the surface amorphous layer. After FIB preparation and polishing procedures, the as-prepared cross-section perovskite specimens were transferred to a high vacuum sputter coater for protection layer deposition. Amorphous carbon layers with a thickness of 10 nm were coated on both sides of the cross-section specimen using pulsed carbon evaporation at 8×10^{-5} mbar. STEM observations of the perovskite cross-section specimens were carried out in an aberration-corrected scanning electron microscope (Titan G2 60-300, Thermo Fisher equipped with a field emission gun) with 300 kV acceleration voltage. The beam current of the electron probe was reduced to 5 pA to minimize the damage to perovskite during high-resolution imaging. The probe convergence angle was 24.5 mrad, and the angular range of the HAADF detector was from 79.5 to 200 mrad. Static GIWAXS measurements were performed at the BL14B1 beamline of the Shanghai Synchrotron Radiation Facility using X-ray with a wavelength of 1.24 Å and a grazing-incidence angle of 0.2°. A 2D XRD pattern was obtained by MarCCD at an exposure time of 10 s at about 342 mm from the sample. The XRD patterns were analyzed using FIT2D software and displayed in the scattering vector q coordinates. In-situ GIWAXS measurements to monitor the stability of perovskite films were performed at beamline sector 12-ID-D at the Advanced Photon Source in Argonne National Laboratory, with 20 KeV incident X-rays and a Pilatus 100 K detector located at ~135 mm from the samples. To reduced air/moisture exposure effects, all samples were mounted in a sealed thin film cell with inert He gas flowing during the stability measurements. The scattering patterns were obtained at an X-ray incident angle of 0.15−0.18 degrees with respect to the sample plane. The surface profiles we tested with a step profilometer (Dektak XT, Bruker, Germany).

Spectroscopic Characterization. UV−vis optical absorption spectra were recorded using a spectroscope (JASCO V-770EX, Japan). $J-V-L$ curves were collected by a spectrometer (Photonic Multichannel Analyzer PMA-12, Hamamatsu, Japan) in combination with a source meter (Keithley 2400, Tektronix, USA). PL spectra were acquired by a Princeton spectrometer (Acton SpectraPro SP-2300, Teledyne Princeton Instruments, USA) with a femtosecond laser (400 nm, 0.12 $\mu J \cdot cm^{-2}$). TRPL spectra were recorded with a Hamamatsu streak camera system which has an ultimate temporal resolution of 1 ps. TA spectra were measured by the HELIOS TA system. In the measurements of PL, TRPL, and TA spectra, the laser source was the Coherent Legend regenerative amplifier (100 fs, 1 kHz, 400 nm) seeded by a Coherent Vitesse oscillator (100 fs, 80 MHz). The excitation beams were incident from top surfaces of perovskite films. The pump fluences in PL, TRPL, and TA measurements were 0.12, 0.12, and 0.32 $\mu J/cm^2$, respectively. PLQY values were recorded with a commercialized system (XPQY-EQE-350-1100, Guangzhou Xi Pu Optoelectronic Technology Co., Ltd., China) with 405 nm laser excitation.

Fabrication and Testing of PeLED Devices. Patterned ITO glasses were sequentially washed with diluted detergent, deionized water and ethanol followed by oxygen plasma treatment for 10 min. The PEDOT:PSS suspension was spin-coated onto ITO glasses at 4000 rpm for 40 s and then at 120 °C for 30 min in ambient atmosphere. Then, the PEDOT:PSS-coated ITO glass substrates were transferred into a nitrogen-filled glove box. Perovskite films were deposited onto the PEDOT:PSS layer as described above. Finally, TPBi (40 nm), LiF (1 nm), and Al (80 nm) were sequentially deposited using thermal evaporation with a shadow mask. The active device area is 2×2.5 mm^2. The $J-V-L$ curves of PeLEDs were tested with a source meter (Keithley 2400, Tektronix, USA) and a spectrometer (Photonic Multichannel Analyzer PMA-12, Hamamatsu, Japan).

ASSOCIATED CONTENT

Supporting Information

The Supporting Information is available free of charge at https://pubs.acs.org/doi/10.1021/acs.chemmater.2c02340.

Energy level diagrams, surface height profiles, additional STEM images, additional GIWAXS results, in-situ monitored XRD patterns, TA spectra, fitted parameters for the TRPL curves, low-temperature PL analysis, PB kinetics, and additional PL results (PDF)

https://doi.org/10.1021/acs.chemmater.2c02340
Chem. Mater. 2022, 34, 10435−10442

AUTHOR INFORMATION

Corresponding Authors

Yuanyuan Zhou − *Department of Physics, Hong Kong Baptist University, Hong Kong SAR 999077, China;* orcid.org/0000-0002-8364-4295; Email: yyzhou@hkbu.edu.hk

Guichuan Xing − *Joint Key Laboratory of the Ministry of Education, Institute of Applied Physics and Materials Engineering, University of Macau, Taipa, Macau 999078, China;* orcid.org/0000-0003-2769-8659; Email: gcxing@um.edu.mo

Authors

Tanghao Liu − *Joint Key Laboratory of the Ministry of Education, Institute of Applied Physics and Materials Engineering, University of Macau, Taipa, Macau 999078, China; Department of Physics, Hong Kong Baptist University, Hong Kong SAR 999077, China*

Qi Wei − *Joint Key Laboratory of the Ministry of Education, Institute of Applied Physics and Materials Engineering, University of Macau, Taipa, Macau 999078, China*

Songhua Cai − *Department of Physics, The Hong Kong Polytechnic University, Hong Kong SAR 999077, China;* orcid.org/0000-0003-3839-2030

Bingchen He − *Joint Key Laboratory of the Ministry of Education, Institute of Applied Physics and Materials Engineering, University of Macau, Taipa, Macau 999078, China*

Zhenhuang Su − *Shanghai Synchrotron Radiation Facility, Zhangjiang Laboratory, Shanghai Advanced Research Institute, Chinese Academy of Sciences, Shanghai 201204, China*

Zhipeng Zhang − *Joint Key Laboratory of the Ministry of Education, Institute of Applied Physics and Materials Engineering, University of Macau, Taipa, Macau 999078, China*

Yalan Zhang − *Department of Physics, Hong Kong Baptist University, Hong Kong SAR 999077, China*

Hua Zhou − *Advanced Photon Source, Argonne National Laboratory, Lemont, Illinois 60439, United States;* orcid.org/0000-0001-9642-8674

Gang Wang − *Joint Key Laboratory of the Ministry of Education, Institute of Applied Physics and Materials Engineering, University of Macau, Taipa, Macau 999078, China*

Yulan Huang − *Joint Key Laboratory of the Ministry of Education, Institute of Applied Physics and Materials Engineering, University of Macau, Taipa, Macau 999078, China*

Jiahao Ren − *Joint Key Laboratory of the Ministry of Education, Institute of Applied Physics and Materials Engineering, University of Macau, Taipa, Macau 999078, China*

Complete contact information is available at: https://pubs.acs.org/10.1021/acs.chemmater.2c02340

Author Contributions

#T.L., Q.W., and S.C. contributed equally to this work.

Notes

The authors declare no competing financial interest.

ACKNOWLEDGMENTS

The authors acknowledge financial support from The Macau Science and Technology Development Fund, Macau SAR (File no. FDCT-0044/2020/A1, FDCT-091/2017/A2, and FDCT-014/2017/AMJ), Research Grants (MYRG2018-00148-IAPME) from the University of Macau, the Natural Science Foundation of China (61904152 and 61935017), Natural Science Foundation of Guangdong Province, China (2019A1515012186), and Guangdong-Hong Kong-Macao Joint Laboratory of Optoelectronic and Magnetic Functional Materials (2019B121205002). Y.Z. acknowledges the Early Career Scheme (22300221) from the Hong Kong Research Grant Council (RGC). Y.Z. also acknowledges the startup grants, the Initiation Grant − Faculty Niche Research Areas (IG-FNRA) 2020/21 and the Interdisciplinary Research Matching Scheme (IRMS) 2020/21 of HKBU. This research used resources of the Advanced Photon Source, U.S. Department of Energy (DOE) Office of Science User Facility operated for the DOE Office of Science by Argonne National Laboratory under Contract No. DE-AC02-06CH11357. S.C. acknowledges the startup grants from the Department of Applied Physics, the Hong Kong Polytechnic University (1-BD96), the General Research Fund (15306021) from the Hong Kong RGC, the National Natural Science Foundation of China (12104381), and the open subject of National Laboratory of Solid State Microstructures, Nanjing University (M34001).

REFERENCES

(1) Cho, H.; Jeong, S.-H.; Park, M.-H.; Kim, Y.-H.; Wolf, C.; Lee, C.-L.; Heo Jin, H.; Sadhanala, A.; Myoung, N.; Yoo, S.; Im Sang, H.; Friend Richard, H.; Lee, T.-W. Overcoming the electroluminescence efficiency limitations of perovskite light-emitting diodes. *Science* **2015**, *350*, 1222−1225.

(2) Guo, Z.; Zhang, Y.; Wang, B.; Wang, L.; Zhou, N.; Qiu, Z.; Li, N.; Chen, Y.; Zhu, C.; Xie, H.; Song, T.; Song, L.; Xue, H.; Tao, S.; Chen, Q.; Xing, G.; Xiao, L.; Liu, Z.; Zhou, H. Promoting Energy Transfer via Manipulation of Crystallization Kinetics of Quasi-2D Perovskites for Efficient Green Light-Emitting Diodes. *Adv. Mater.* **2021**, *33*, No. 2102246.

(3) Liu, X.-K.; Xu, W.; Bai, S.; Jin, Y.; Wang, J.; Friend, R. H.; Gao, F. Metal halide perovskites for light-emitting diodes. *Nat. Mater.* **2021**, *20*, 10−21.

(4) Ma, D.; Lin, K.; Dong, Y.; Choubisa, H.; Proppe, A. H.; Wu, D.; Wang, Y.-K.; Chen, B.; Li, P.; Fan, J. Z.; Yuan, F.; Johnston, A.; Liu, Y.; Kang, Y.; Lu, Z.-H.; Wei, Z.; Sargent, E. H. Distribution control enables efficient reduced-dimensional perovskite LEDs. *Nature* **2021**, *599*, 594−598.

(5) Tan, Z.-K.; Moghaddam, R. S.; Lai, M. L.; Docampo, P.; Higler, R.; Deschler, F.; Price, M.; Sadhanala, A.; Pazos, L. M.; Credgington, D.; Hanusch, F.; Bein, T.; Snaith, H. J.; Friend, R. H. Bright light-emitting diodes based on organometal halide perovskite. *Nat. Nanotechnol.* **2014**, *9*, 687−692.

(6) Wang, N.; Cheng, L.; Ge, R.; Zhang, S.; Miao, Y.; Zou, W.; Yi, C.; Sun, Y.; Cao, Y.; Yang, R.; Wei, Y.; Guo, Q.; Ke, Y.; Yu, M.; Jin, Y.; Liu, Y.; Ding, Q.; Di, D.; Yang, L.; Xing, G.; Tian, H.; Jin, C.; Gao, F.; Friend, R. H.; Wang, J.; Huang, W. Perovskite light-emitting diodes based on solution-processed self-organized multiple quantum wells. *Nat. Photonics* **2016**, *10*, 699−704.

(7) Xing, G.; Mathews, N.; Lim, S. S.; Yantara, N.; Liu, X.; Sabba, D.; Grätzel, M.; Mhaisalkar, S.; Sum, T. C. Low-temperature solution-processed wavelength-tunable perovskites for lasing. *Nat. Mater.* **2014**, *13*, 476−480.

(8) Yang, X.; Zhang, X.; Deng, J.; Chu, Z.; Jiang, Q.; Meng, J.; Wang, P.; Zhang, L.; Yin, Z.; You, J. Efficient green light-emitting diodes

based on quasi-two-dimensional composition and phase engineered perovskite with surface passivation. *Nat. Commun.* **2018**, *9*, 570.
(9) Liu, Z.; Qiu, W.; Peng, X.; Sun, G.; Liu, X.; Liu, D.; Li, Z.; He, F.; Shen, C.; Gu, Q.; Ma, F.; Yip, H.-L.; Hou, L.; Qi, Z.; Su, S.-J. Perovskite Light-Emitting Diodes with EQE Exceeding 28% through a Synergetic Dual-Additive Strategy for Defect Passivation and Nanostructure Regulation. *Adv. Mater.* **2021**, *33*, No. 2103268.
(10) Jin, G.; Zhang, D.; Pang, P.; Ye, Z.; Liu, T.; Xing, G.; Chen, J.; Ma, D. Boosting the performance of CsPbBr3-based perovskite light-emitting diodes via constructing nanocomposite emissive layers. *J. Mater. Chem. C* **2021**, *9*, 916−924.
(11) Xing, G.; Wu, B.; Wu, X.; Li, M.; Du, B.; Wei, Q.; Guo, J.; Yeow, E. K. L.; Sum, T. C.; Huang, W. Transcending the slow bimolecular recombination in lead-halide perovskites for electroluminescence. *Nat. Commun.* **2017**, *8*, No. 14558.
(12) Yuan, M.; Quan, L. N.; Comin, R.; Walters, G.; Sabatini, R.; Voznyy, O.; Hoogland, S.; Zhao, Y.; Beauregard, E. M.; Kanjanaboos, P.; Lu, Z.; Kim, D. H.; Sargent, E. H. Perovskite energy funnels for efficient light-emitting diodes. *Nat. Nanotechnol.* **2016**, *11*, 872−877.
(13) Liu, T.; Zhang, Z.; Wei, Q.; Wang, B.; Wang, K.; Guo, J.; Liang, C.; Zhao, D.; Chen, S.; Tang, Y.; Zhou, Y.; Xing, G. Tailoring quasi-2D perovskite thin films via nanocrystals mediation for enhanced electroluminescence. *Chem. Eng. J.* **2021**, *411*, No. 128511.
(14) Kong, L.; Zhang, X.; Li, Y.; Wang, H.; Jiang, Y.; Wang, S.; You, M.; Zhang, C.; Zhang, T.; Kershaw, S. V.; Zheng, W.; Yang, Y.; Lin, Q.; Yuan, M.; Rogach, A. L.; Yang, X. Smoothing the energy transfer pathway in quasi-2D perovskite films using methanesulfonate leads to highly efficient light-emitting devices. *Nat. Commun.* **2021**, *12*, 1246.
(15) Sun, C.; Jiang, Y.; Cui, M.; Qiao, L.; Wei, J.; Huang, Y.; Zhang, L.; He, T.; Li, S.; Hsu, H.-Y.; Qin, C.; Long, R.; Yuan, M. High-performance large-area quasi-2D perovskite light-emitting diodes. *Nat. Commun.* **2021**, *12*, 2207.
(16) Li, G.; Song, J.; Wu, J.; Song, Z.; Wang, X.; Sun, W.; Fan, L.; Lin, J.; Huang, M.; Lan, Z.; Gao, P. Efficient and Stable 2D@3D/2D Perovskite Solar Cells Based on Dual Optimization of Grain Boundary and Interface. *ACS Energy Lett.* **2021**, *6*, 3614−3623.
(17) Kim, H.; Kim, J. S.; Heo, J.-M.; Pei, M.; Park, I.-H.; Liu, Z.; Yun, H. J.; Park, M.-H.; Jeong, S.-H.; Kim, Y.-H.; Park, J.-W.; Oveisi, E.; Nagane, S.; Sadhanala, A.; Zhang, L.; Kweon, J. J.; Lee, S. K.; Yang, H.; Jang, H. M.; Friend, R. H.; Loh, K. P.; Nazeeruddin, M. K.; Park, N.-G.; Lee, T.-W. Proton-transfer-induced 3D/2D hybrid perovskites suppress ion migration and reduce luminance overshoot. *Nat. Commun.* **2020**, *11*, 3378.
(18) Jang, Y.-W.; Lee, S.; Yeom, K. M.; Jeong, K.; Choi, K.; Choi, M.; Noh, J. H. Intact 2D/3D halide junction perovskite solar cells via solid-phase in-plane growth. *Nat. Energy* **2021**, *6*, 63−71.
(19) Xiao, X.; Wang, K.; Ye, T.; Cai, R.; Ren, Z.; Wu, D.; Qu, X.; Sun, J.; Ding, S.; Sun, X. W.; Choy, W. C. H. Enhanced hole injection assisted by electric dipoles for efficient perovskite light-emitting diodes. *Commun. Mater.* **2020**, *1*, 81.
(20) Yu, X.; Liu, T.; Wei, Q.; Liang, C.; Wang, K.; Guo, J.; Zhao, D.; Wang, B.; Chen, R.; Xing, G. Tailoring the Surface Morphology and Phase Distribution for Efficient Perovskite Electroluminescence. *J. Phys. Chem. Lett.* **2020**, *11*, 5877−5882.
(21) Yang, G.; Liu, X.; Sun, Y.; Teng, C.; Wang, Y.; Zhang, S.; Zhou, H. Improved current efficiency of quasi-2D multi-cation perovskite light-emitting diodes: the effect of Cs and K. *Nanoscale* **2020**, *12*, 1571−1579.
(22) Zou, C.; Liu, Y.; Ginger, D. S.; Lin, L. Y. Suppressing Efficiency Roll-Off at High Current Densities for Ultra-Bright Green Perovskite Light-Emitting Diodes. *ACS Nano* **2020**, *14*, 6076−6086.
(23) Shen, Y.; Shen, K.-C.; Li, Y.-Q.; Guo, M.; Wang, J.; Ye, Y.; Xie, F.-M.; Ren, H.; Gao, X.; Song, F.; Tang, J.-X. Interfacial Potassium-Guided Grain Growth for Efficient Deep-Blue Perovskite Light-Emitting Diodes. *Adv. Funct. Mater.* **2021**, *31*, No. 2006736.
(24) Yang, F.; Chen, H.; Zhang, R.; Liu, X.; Zhang, W.; Zhang, J.; Gao, F.; Wang, L. Efficient and Spectrally Stable Blue Perovskite Light-Emitting Diodes Based on Potassium Passivated Nanocrystals. *Adv. Funct. Mater.* **2020**, *30*, No. 1908760.
(25) Abdi-Jalebi, M.; Andaji-Garmaroudi, Z.; Cacovich, S.; Stavrakas, C.; Philippe, B.; Richter, J. M.; Alsari, M.; Booker, E. P.; Hutter, E. M.; Pearson, A. J.; Lilliu, S.; Savenije, T. J.; Rensmo, H.; Divitini, G.; Ducati, C.; Friend, R. H.; Stranks, S. D. Maximizing and stabilizing luminescence from halide perovskites with potassium passivation. *Nature* **2018**, *555*, 497−501.
(26) Cai, S.; Dai, J.; Shao, Z.; Rothmann, M. U.; Jia, Y.; Gao, C.; Hao, M.; Pang, S.; Wang, P.; Lau, S. P.; Zhu, K.; Berry, J. J.; Herz, L. M.; Zeng, X. C.; Zhou, Y. Atomically Resolved Electrically Active Intragrain Interfaces in Perovskite Semiconductors. *J. Am. Chem. Soc.* **2022**, *144*, 1910−1920.
(27) Ali, M. U.; Cai, W.; Cai, J.; Miao, J.; Zhang, S.; Chen, J.; Xiao, L.; Meng, H.; Yan, C.; Wei, G. Enabling Quasi-2D Perovskite-Compatible Growth Environment for Efficient Light-Emitting Diodes. *Adv. Opt. Mater.* **2022**, *10*, No. 2100671.
(28) Gong, J.; Hao, M.; Zhang, Y.; Liu, M.; Zhou, Y. Layered 2D Halide Perovskites beyond the Ruddlesden−Popper Phase: Tailored Interlayer Chemistries for High-Performance Solar Cells. *Angew. Chem., Int. Ed.* **2022**, *61*, No. e202112022.
(29) Zhou, Y.; Herz, L. M.; Jen, A. K-Y.; Saliba, M. Advances and challenges in understanding the microscopic structure−property−performance relationship in perovskite solar cells. *Nature Energy* **2022**, *7*, 794−807.
(30) Gong, X.; Voznyy, O.; Jain, A.; Liu, W.; Sabatini, R.; Piontkowski, Z.; Walters, G.; Bappi, G.; Nokhrin, S.; Bushuyev, O.; Yuan, M.; Comin, R.; McCamant, D.; Kelley, S. O.; Sargent, E. H. Electron−phonon interaction in efficient perovskite blue emitters. *Nat. Mater.* **2018**, *17*, 550−556.
(31) Du, Q.; Zhu, C.; Yin, Z.; Na, G.; Cheng, C.; Han, Y.; Liu, N.; Niu, X.; Zhou, H.; Chen, H.; Zhang, L.; Jin, S.; Chen, Q. Stacking Effects on Electron−Phonon Coupling in Layered Hybrid Perovskites via Microstrain Manipulation. *ACS Nano* **2020**, *14*, 5806−5817.
(32) Jiang, Y.; Cui, M.; Li, S.; Sun, C.; Huang, Y.; Wei, J.; Zhang, L.; Lv, M.; Qin, C.; Liu, Y.; Yuan, M. Reducing the impact of Auger recombination in quasi-2D perovskite light-emitting diodes. *Nat. Commun.* **2021**, *12*, 336.

https://doi.org/10.1021/acs.chemmater.2c02340
Chem. Mater. 2022, 34, 10435−10442